Improving 3D water column seismic imaging using the Common Reflection Surface method

Parsa Bakhtiari Rad[1] and Leonardo Macelloni[2*]

1 National Center for Physical Acoustic (NCPA). The University of Mississippi. 145 Hill Drive, University Campus, 38677 MS, USA

2 Hydrographic Science Research Center. School of Ocean Science & Engineering. The University of Southern Mississippi. 1020 Balch Blvd., Stennis Space Center, MS 39529-9904.

*Corresponding author: leonardo.macelloni@usm.edu

ABSTRACT

Water column processing has gained attention in recent years since a seismic model of a water column could assist marine data processors to correctly image the sub-seafloor geology, which is the target of primary interest. In addition to seismic processing, water column imaging has gained interest in the physical oceanography community for improved study of oceanographic processes. However, seismic water column processing is challenging since the internal reflections of the ocean are inherently weak and are often masked by noise. In this work, we adopt the common reflection surface stack technique in order to improve the imaging of ocean water layers. The common reflection surface stack is a robust data preconditioning and stacking technique in seismic processing that relies on the kinematic wavefront attributes of seismic waves. The method is applied to a multichannel 3D data set collected for oil and gas exploration in the deep-water Gulf of Mexico. The method greatly improves inline sections but does not significantly enhance crosslines and horizontal slices, which are more sensitive to both the acquisition geometry and the temporal variability of ocean water masses.

Key words: CRS; water column; 3-D seismic imaging; seismic oceanography.

1 Introduction

Water column processing could deliver important information about the effect of water masses on subsurface data processing in order to improve final imaging. Although water column processing is not included in standard processing, it is gaining attention recently. For 2D and 3D common-midpoint (CMP) imaging surveys, we typically use a single water column velocity profile and treat any spatial or temporal variations as static shifts applied as needed in the processing flow (Lacombe et al., 2009). In 4D surveys, it is important to separate the temporal variations in these static corrections from those we can attribute to other mechanisms such as the source-consistent statics related to the source radiation pattern and source tow, or the receiver-consistent statics associated with the near-seafloor geology (MacKay et al., 2003). In a full-waveform inversion study, where the goal is to create a high-resolution subsurface velocity model, it is implied that a water column velocity model must be created that accounts for any variations in the raypaths within the water column which obscure the variations of interest in our target (i.e., Wood et al., 2008; Benfield et al., 2017). As the requirements of spatial or temporal resolution increase, processing is forced to increase the resolution and complexity of water column models to more accurately represent their heterogeneity.

In the field known as seismic oceanography, the goal of the imaging exercise is to apply the techniques of reflection seismology to the water column itself. Scientists attempt to spatially and temporally map the changes in the water column impedance, which represents variations in salinity, temperature, pressure and density, to gain insight into the ocean processes which drive the stratification and variability of the water column. Holbrook et al. (2003) first showed that 2D seismic reflection sections, if appropriately processed, provide high resolution images of the ocean structures. Successively, Nandi et al. (2004) demonstrated that reflections within the water column are well-correlated with temperature contrasts and that water velocity is mainly influenced by temperature variations, and to a lesser extent, by salinity and density. These initial studies prompted physical oceanographers and geophysicists to investigate ocean water column physics using seismic data and, since then, seismic imaging and inversion have been proven to be useful tools in investigating oceanographic processes such as internal waves (Dickinson et al., 2017); thermohaline structures (Ruddick et al., 2009; Papenberg et al., 2010); and fronts, eddies and boundaries between different water masses (Mirshak et al., 2010; Pinheiro et al., 2010). However, to date, the preponderance of seismic oceanography studies have used 2D seismic data, while 3D seismic data has been only minimally exploited by processing individual 2D swath subsets of 3D data (Blacic and Holbrook, 2010). In seismic oceanography applications, the water column acoustic impedance changes are on the order of 100 to 1000 times weaker than those occurring in the solid earth; in terms of dynamic range, this requires processing to achieve 20-30 dB of gain when using conventional seismic data acquisition technologies. Reflections in the water column are readily masked by both coherent noise (e.g., direct wave, swell noise, subsurface reflections, strum noise) and non-coherent noise mechanisms (Holbrook et al., 2003; Piete et al., 2013). The operational limits of acquisition are a very confining factor in data processing since the acquisition is designed for subsurface imaging. Information theory assumes that with enough data and the correct processing model, these signals could be recovered from noise with sufficient processing gain. However, this may be beyond the limits of practicality in all cases for a given data set.

In this work, we present enhanced 3D seismic images of the water column obtained by implementing a processing workflow based on the common-reflection-surface (CRS) technique. We evaluate the performance of the 3D CRS method on the water portion of a 3D multichannel seismic data set collected in the deep water of the Gulf of Mexico for oil and gas exploration. The results of the 3D CRS are compared with results of the standard 3D CMP to highlight the improvements.

The CRS imaging is a data-driven and robust tool in seismic data processing that is particularly suitable for imaging of weak reflections (Müller, 1999; Jäger et al., 2001; Mann, 2002). We implement the CRS-based workflows in prestack and poststack domains to improve the quality and continuity of the reflections within the water column. The prestack data enhancement is handled by the partial CRS method (Baykulov and Gajewski, 2009) which is a robust method for data preconditioning and interpolation.

The standard CMP stack is based on the estimation of the root-mean-square (RMS) velocities that are usually obtained by manual picking of semblance panels, and as such is highly user-dependent. In turn, the CRS stack requires less user input, as the main user-selected parameter is the choice of the aperture size for data stacking in different domains. The semblance bandwidth and a rough estimate of the near-surface velocity must be defined by the user as well. In the CRS technique no prior information about the media interior is required for processing. Therefore, we believe this method is well-suited for modeling the variations in oceanic water velocity, which are small in absolute magnitude but widely varying in space.

2 Theory background

2.1 The Common-Reflection-Surface Stack

The CRS stack operator is based on wavefront curvature attributes (Hubral, 1983; Schleicher et al., 1993) and has many applications in seismic data processing including multiple suppression (Dümmong and Gajewski, 2008), velocity model building (Duveneck, 2004; Bakhtiari Rad et al., 2015; Bauer et al., 2016), diffraction separation (Dell and Gajewski, 2011; Bakhtiari Rad et al., 2018; Bakhtiari Rad et al., 2018; Schwarz, 2019), seismology in crystaline environment (Ahmed et al., 2015), near-surface processing (Bakhtiari Rad and Hickey, 2019), data interpolation (Baykulov and Gajewski, 2009) to name a few. The common-reflection-surface (CRS) method is a multi-parameter stacking technique that, in contrast to the CMP stack (Mayne, 1962), includes many neighboring CMPs. The hyperbolic 2D zero-offset CRS stack operator is parameterized in terms of the CRS parameters from Hubral (1983) in equation form by Schleicher et al. (1993) and Jäger et al. (2001) as:

$$t^2_{\mathrm{CRS}}(\Delta x_m, h) = \left(t_0 + \frac{2\sin\alpha}{v_0}\Delta x_m\right)^2 + \frac{2t_0\cos^2\alpha}{v_0}\left(\frac{\Delta x_m^2}{R_{\mathrm{N}}} + \frac{h^2}{R_{\mathrm{NIP}}}\right) \quad . \qquad (1)$$

Equation 1 describes the stacking traveltime t_{CRS} in the vicinity of the CMP location x_0 in the midpoint $\Delta x_m = x_m - x_0$ and half-offset (h) coordinates, given the zero-offset traveltime t_0 and near-surface velocity v_0. The three surface-related CRS parameters are the incidence/emergence angle at the coinciding central source and receiver locations (α), the radius of wavefront curvature due to a fictitious point source at the normal-incidence point (NIP) on the reflector (R_{NIP}), and the radius of the wavefront curvature from a notional exploding reflector element surrounding the NIP on the common-reflection-surface R_N as shown in Figure 1. As such, t_{CRS} may be used to coherently stack data on the reflection surface.

2.2 Partial Common-Reflection-Surface Stack

The CRS method may be implemented as a partial prestack operation (Baykulov and Gajewski, 2009) for prestack data enhancement, data interpolation and offset regularization. Figure 2 illustrates the CRS and partial CRS surfaces. The partial CRS makes use of the same zero-offset CRS parameters to calculate the local stacking surface. To implement the partial CRS, the zero-offset time t0 of every finite-offset sample is estimated as:

$$t_0 = -\frac{h^2 \cos^2 \alpha}{v_0 R_{NIP}} + \sqrt{\left(\frac{h^2 \cos^2 \alpha}{v_0 R_{NIP}}\right)^2 + t^2(\Delta x_m, h)} \qquad (2)$$

with the finite-offset traveltime of the arbitrary sample as $t(\Delta x_m, h)$. The other parameters in the above equation are the same parameters as in the Equation 1. The estimated t_0 can be found in a minimization procedure detailed in Baykulov and Gajewski (2009). Depending on the aperture size of the partial CRS, the number of traces used during the partial stacking may vary. Therefore, the constructive summation of coherent events leads to prestack data enhancement. Partial CRS stack has found interesting applications in seismic data interpolation and regularization (e.g., Baykulov and Gajewski, 2009; Bakhtiari Rad, 2016).

2.3 3D Common-Reflection-Surface Extension

As with the 2D zero-offset CRS stacking operator, the 3D version can be derived from paraxial ray theory assuming a mild lateral variation in the overburden. 3D CRS traveltime is expressed in terms of the zero-offset wavefront attributes and it is given (e.g., Bergler, 2004) by:

$$t^2_{\mathrm{CRS}}(\Delta \mathbf{x}_m, \mathbf{h}) = (t_0 + 2\mathbf{p}\Delta \mathbf{x}_m)^2 + 2\,t_0\left(\Delta \mathbf{x}_m^{\mathbf{T}} \mathbf{M}_{\mathrm{N}} \Delta \mathbf{x}_m + \mathbf{h}^{\mathbf{T}} \mathbf{M}_{\mathrm{NIP}} \mathbf{h}\right) \quad , \qquad (3)$$

where $\mathbf{M}_{NIP}$ and $\mathbf{M}_N$ are symmetric 2 × 2 matrices that describe the wavefront curvatures of the normal and NIP waves, respectively, **p** is the slowness vector in terms of incident angle α and azimuth β, the half-distance vector between shot and receiver coordinates is h, and Δx_m is the midpoint displacement vector with respect to the central ray coordinate. Accordingly, there are eight parameters for a 3D CRS stack operator: three R_{NIP} components, three R_N components and two angles α, and β. More details on the 3D extension of the CRS method are found in Bergler (2004); Bakhtiari Rad et al. (2015) and Xie and Gajewski (2016).

The estimation of the 3D CRS parameters is a typical problem of global optimization (e.g., Bonomi et al., 2009). In general, for each sample in the zero-offset volume, the eight parameters of the 3D CRS must be estimated such that they provide the highest coherence for the data that is summed up along the stacking surface. However, since a global eight-parameter estimation is computationally too expensive, a pragmatic and less-expensive approach that splits the eight-parameter estimation into three independent searches in the sub-volumes of the data was suggested by Müller (2003) and Bergler (2004). The pragmatic approach (PA) is composed of an initial search and a local optimization scheme. After initial search is carried out, an initial CRS stack volume is obtained. For further improvement of the stack, the initial stacking parameters can be refined using an optimization technique, e.g., simulated annealing (SA) as proposed by Müller (2003). The pragmatic approach is fast and reliable in mild areas with no sharp change in velocity. However, in geologically complex areas, the attribute-search algorithm might fail when many local extrema are present. In recent years, some global optimization algorithms have been tested to estimate the 3D CRS parameters simultaneously (e.g., Xie and Gajewski, 2016; Garabito, 2018). Despite promising results, they are still expensive and hard to implement. In the framework of this project, we used the classical pragmatic approach followed by a local optimization suggested by Müller (2003) and improved by Xie and Gajewski (2018) to partially account for conflicting dips.

3 Data and method

3.1 Data

The seismic data used in this study are a portion of a larger multiclient 3D seismic survey MC 14-Q carried out by Schlumberger-Western Geco in the Northern Gulf of Mexico between 2002 and 2003. Seismic lines were acquired using a 5085 in^3 dual source air gun with a source separation of 50 m and shot spacing of 37.5 m for both sources acquired in a flip-flop shooting pattern. The receivers were in eight streamers of eight km length towed at a 100 m spacing. The number of receivers was 640 per streamer with the group interval of 12.5 m. The total number of receivers per shot is 5120. The sample rate was 2 milliseconds with the Nyquist frequency of 250 Hz. The record length is 12 seconds and the nominal fold was 64. According to the acquisition reports the sea surface conditions were calm throughout data acquisition. The survey vessel maintained a velocity near 5 knots (2.5 m/s) running NW-SE survey lines (i.e., inline azimuth of 330°) over a gentle seafloor slope ranging from 800 to 1300 m water depth. For this study we received 50 swaths covering an area of approximately 15 km × 15 km, including Mississippi Canyon lease blocks 73, 74, 75, 117, 118, 119, 161, 162, and 163 (Figure 3).We received only the water column portion of the seismic traces, which were muted out below the mud line.

3.1 Data selection and preprocessing

Data preprocessing was carried out before applying both the standard CMP and CRS imaging workflows. After initial data analysis, trace editing and amplitude balancing were performed. Data showed a dominant frequency of 65 Hz. Because long offsets are not useful for imaging within the water column, traces with offsets greater than 4500 m were excluded from preprocessing. The data were muted at the seafloor reflection to achieve a relative balance of average amplitude levels of the remaining data containing the water column reflections of interest. The data preprocessing used here employed standard techniques for subsurface seismic imaging adapted to work with the water-column specific issues. In the data of interest (the data above the first arrival from the seafloor), many of the noise sources are related to the acquisition itself, such as air gun bubbles, direct arrivals from the source, ships engines, and reflection energy returns from previous shots. Other sources of noise in the environment include wind, shipping activity, and inherent ocean noise. A low-cut band pass filter with frequency of 5 Hz attenuated most of low frequency noise. Given the various noise mechanisms, we needed to carefully design a filtering strategy specifically tailored to remove or minimize as much noise as possible while preserving the weak signals. For example, removing the direct source-to-receiver wave was one of the most difficult noise sources to address in this process. The direct waves directly overlap the subtle internal reflections of the water column and complicate the imaging. The frequency-wavenumber (FK) filters were applied in different data domains (e.g., common shot gather, common offset gather) to attenuate the direct waves. Furthermore, we employed Radon-domain filtering followed by adaptive subtraction. A band pass filter of 5 to 150 Hz was repeatedly applied after each processing step to attenuate high frequency noise and spikes. The final step in preprocessing was a gain correction for spherical divergence. The preprocessed data were then prepared for velocity analysis and stacking.

3.3 CMP stack and CRS stack

The CMP stack was obtained after velocity analysis using semblance panels within a dense grid of 250 m spacing in the inline and 100 m in the crossline line direction. In general, the stacking velocities varied from 1410 to 1590 m/s. The normal-moveout (NMO) correction (Yilmaz, 2001) and stacking were carried out assuming the native survey bin size of 6.25 m crossline and 25 m inline with no traces interpolation. The semblance panels were picked manually since the velocity variations within the water column were small and prone failure by automatic picking. One of the complications of stack reflections within the water column is the time scale over which thermohaline variations can occur, which may be shorter than that of the data acquisition window. Klaeschen et al. (2009) demonstrated that when considering survey vessels with standard acquisition speeds of about 2 m/s, the very narrow range of sound velocity variability in the water and the very small reflections dips, water column reflectors do not move during the shot and the recording of the reflected signal and 2D seismic lines are a correct snapshot representation of water conditions. Blacic and Holbrook (2010) demonstrated that a single seismic swath in a large 3D oilfield survey is not affected by water column reflectors movement and that CMP stacking can be applied to the seismic data. Alternatively, water conditions can vary from swath to swath altering

continuity of reflections and in which case the time effect must be considered when stacking the entire volume.

Unlike with a standard subsurface imaging exercise, when we created our 3D CRS supergathers, we had to consider both the spatial distribution of the traces as well as the time of acquisition. Recalling that the survey spanned more than six months and considering the temporal variability of the imaging targets as detailed above, we needed to add both time and spatial selection criteria for the gather design. As such, we created supergathers spanning 1000 m in the inline direction, 100 m in the crossline direction, and removed traces that were not judged to fall within a time window that we could reasonably assert represented a single snapshot of the environment.

4 Imaging Results

In order to test the capability of CRS workflow in enhancing seismic images of the water column, CRS results are compared with the standard CMP method at different steps in the data processing, namely CMP and CRS stack gathers, Velocity semblance panels and inlines, crosslines and time slice sections. Results are displayed synoptically in the following sections.

4.1 CMP vs CRS gathers

An example of a CMP gather used as input for the stacking is shown in Figure 4(a). The CMP gather exhibits lower fold and offset gaps due to operational problems during acquisition. The corresponding CRS supergather is shown in Figure 4(b). We used partial CRS to improve the quality of prestack data. The aperture size for partial stacking was determined after some trial and error and was chosen as 300 m along the offset direction and 50 m along the midpoint. This small size helps to improve the quality and infill missing offsets without stacking of traces collected at different times. The CRS supergather shows an enhanced quality. Two large gaps near the 1300 m and 2700 m offset ranges are infilled appropriately. Moreover, because of trace interpolation via partial CRS, the number of traces (fold) in the CRS supergather is almost twice the CMP gather.

4.2 Velocity semblance panels

Improving prestack data using partial CRS not only enhances the stacking, but also the velocity model building. The associated velocity spectrum of CMP gather that is shown in Figure 4(a) is displayed in Figure 5(a). It is observed that the semblance picks are mostly located in a narrow band between 1400 to 1500 m/s. Despite noise and missing samples, the higher semblance values are better focused from 0.3 to 0.8 s in two-way travel time (TWT). Figure 5(b) shows the comparable semblances obtained from the corresponding CRS supergather (Figure 4(b)). This velocity panel exhibits more focused picks with higher semblance values. In the CMP-derived velocity panel, the pick trend is faint and hard to pick below 0.8 s TWT, while the CRS-derived panel exhibits less noise and enhanced picks.

4.3 Inline, crossline and time slice

Figure 6(a) shows the CMP stack section of an arbitrary inline cutting through of the final stacked 3D volume. The section starts at 0.2 s TWT because the top part of the record is missing due to the lack of reflections in the near-offset records (the average minimum offset is 250 m). This is because the acquisition geometry is optimized for deep oil exploration targets and not for water column imaging. In addition to the low fold issue in the near offsets, this portion of the record is the most affected by the signal distortion due to the direct wave suppression. The other portion of the section between 0.4 to 1 s TWT shows clear horizontal reflections due to the ocean temperature and density stratification. For the position below 1 s to the seafloor, it is observed that the seismic data show less uniform layering of the reflections with more chaotic events possibly due to water mixing processes. Figure 6(b) displays the CRS stack of the same inline.

This section exhibits more reflections, especially in the middle parts. The white arrows in Figure 6(b) show some strong reflections that are better imaged using the CRS versus the CMP result in Figure 6(a). The reflected events also have more lateral continuity. This is more evident in the zoomed area in the white box. The deeper portion of the water column is the most enhanced by the CRS workflow, with many new reflectors imaged, short horizons with increased continuity and less random noise overall in the seismic image. Moreover, while with the CMP stack method the shallow signals are muted due to stretch NMO effect (Yilmaz, 2001), the CRS parameters are estimated independently and hence the NMO- stretch effect is less pronounced (note the very shallow area in both sections). The CRS stack performance is poor at the edges of the section. This is because boundary effects deteriorate the CRS parameters determination (Bakhtiari Rad et al., 2015).
A 3D Kirchoff time migration with the RMS velocities estimated from user-picking of the semblances was applied. Afterwards, the data were converted to depth using the same velocities. A short migration aperture in crossline direction was considered to avoid summing up inconsistent traces from two swaths. Poststack filtering was performed to attenuate migration artifacts. A CMP-based crossline is shown in Figure 7(a) while Figure 7(b) shows the CRS results of the same crossline. Overall, water column crosslines show lower quality, acquisition footprint and swath effect produce a noise with vertical pattern and the time effect segments a large part of the reflections. However, by comparing the two results, in particular within the portion of the lines belonging to the same swath or consecutive swaths, it is possible to observe that the CRS processing improves the data and reduces the footprint gaps (note the black arrows). The temporal variability of the ocean is more significant in the shallow portion (from 200 to 400 m) where water is more subject to ocean mixing and seasonal effects than the deep ocean where water masses are more stable over time. Seismic depth slices reflect this process.
Figure 8(a) and Figure 8(b) show the 350 m depth slice obtained using the CMP and CRS processing, respectively. Overall, the footprint affects both images, but edges of the footprint stripes are more smoothed using the CRS-based processing (see the red arrows for comparison). Figure 8(c) and Figure 8(d) show the 650 m depth slice obtained using the CMP and CRS processing, respectively. The signal amplitude's reduce with depth confirms a decreasing temperature gradient. Figure 8(e) and Figure 8(f) show the 850 m depth slice obtained using the CMP and CRS processing, respectively. The area in solid grey is the seafloor. In such deeper parts where water conditions are more stable, the CRS workflow delivers better results especially in terms of reflections consistency and continuity (red arrows). This is further evidenced in Figure 9(a) and Figure 9(b) where a 7.5×6.25×0.4 km^3 sub-volume display the CMP and CRS results, respectively, both in inline and crossline direction. The CRS sub-volume shows higher continuity of the reflections in the water column, in particular for the events close to the seafloor (red arrows).

5 Discussion

We have tried to enhance water column images of 3D seismic data acquired for deeper targets. Water column imaging needs specific processing, in particular to remove the noise affecting the

signal. For 3D data collected for oil exploration purposes, orientation and timing of the survey is essentially random with respect to oceanographic processes. Because a 3D seismic data set may be acquired over several months, thermohaline interfaces can move during data collection. Our results show that, even for very large surveys, water conditions in this region of the Gulf of Mexico appear to be stable during the recording of a single seismic swath. CRS supergathers designed preferentially along the inline directions produce better inlines sections than the equivalent CMP gathers. Crosslines and horizontal slices do not show the same promising results. To address this issue, we suggest that a detailed analysis of time variability should be carried out for the entire volume. For example, the analysis of the correlation among inlines would indicate the portion of the seismic volume with similar water conditions. Using this portion, then the processing workflow could be run on appropriately segmented subsets of data.
Additionally, including independent oceanographic measurements in seismic processing may improve the final image. For example, the stacking velocities can be improved using the information obtained from the Expendable Bathythermograph (XBT) or Conductivity, Temperature Depth (CTD) casts. Those casts are in-situ measurements that contain information about water temperature and salinity that can be inverted to sound speed (Nandi et al., 2004; Ruddick et al., 2009). Moreover, Fortin and Holbrook (2009) showed that including XBT casts in the velocity semblance panel could improve picking and enhance the velocity model building.
In addition to inverting oceanographic casts, a velocity model can also be modeled using the wavefront tomography technique introduced by Duveneck (2004), which is an inversion scheme based on the CRS parameters. In this approach, the NIP-wave is iteratively inverted to produce a consistent velocity model. During the inversion process, a velocity model is found that minimizes the misfits between the modeled and estimated (observed) radius of curvature of NIP wavefront. Higher resolution velocity model building methods, e.g., full waveform inversion (e.g., Pratt, 1999) can also be implemented.

6 Conclusions

We have presented the results of improving water column seismic imaging using 3D multichannel
seismic data collected in the deep-water Gulf of Mexico for oil and gas prospecting. We improved the imaging by applying the common-reflection-surface (CRS) stack technique which had not been previously used for water column imaging. We applied the CRS method in both zero-offset and finite-offset domains to enhance data quality and extract more accurate velocities from weak reflections. Particular care was taken to design appropriate CRS supergathers considering the time varying nature of water reflections. Accordingly, CRS stack parameters have been selected using both temporal and spatial constraints privileging the inline direction. In comparison to CMP stack sections, we observe the CRS technique offers improvements in both pre- and poststack domains. The CRS-processed data have improved acquisition footprint attenuation, increased reflection event continuity, and can image events previously absent in the deeper part of the seismic record. At the moment, our method offers good results for inline

sections, but fails to enhance crosslines and horizontal slices which are more sensitive to both the acquisition geometry and temporal variability of ocean water masses.

Acknowledgments

We would like to thank Zheguang Zou, Yujiang Xie, John D. Anderson and Craig J. Hickey for kind support, suggestions and discussion. The authors are also indebted to Paul E. Murray at the University of Texas Austin for manuscript revisions. The CRS codes used in this work were developed by the Wave Inversion Technology (WIT) consortium, Hamburg, Germany. Seismic Un*x routines developed by the Center for Wave Phenomena (CWP) from the Colorado School of Mines were also used. We are particularly grateful to Schlumberger WesternGeco both for providing the seismic data and for the educational license of Vista. This work was funded by the National Oceanic and Atmospheric Administration, Ocean Exploration and Research (NOAA-OER) grant # NA17OAR0110210.

Bibliography

Ahmed, K. A., B. Schwarz, and D. Gajewski, 2015, Application of the 3D common-reflection-surface stack workflow in a crystalline rock environment: Geophysical Prospecting, 63, 990–998.

Bakhtiari Rad, P., 2016, Processing and imaging of seismic diffraction using multiparameter stacking attributes: PhD thesis, University of Hamburg.

Bakhtiari Rad, P., D. Gajewski, and L. Macelloni, 2018, Diffraction separation based on the projected first Fresnel zone: Journal of Geophysics and Engineering, 15, 2507–2515.

Bakhtiari Rad, P., D. Gajewski, and C. Vanelle, 2015, 3-D time migration velocity model building using CRS-based pre-stack diffraction separation: SEG Technical Program Expanded Abstracts, 4091–4095.

Bakhtiari Rad, P., and C. J. Hickey, 2019, Improving optimum-offset data for near-surface reflection surveying using a multi-parameter stacking scheme: 89th SEG Technical Program Expanded Abstract.

Bakhtiari Rad, P., B. Schwarz, C. Vanelle, and D. Gajewski, 2018, Common-reflection-surface-based prestack diffraction separation and imaging: Geophysics, 83, S47–S55.

Bauer, A., B. Schwarz, and D. Gajewski, 2016, Improving the resolution of wavefront tomography by utilizing diffractions: SEG Technical Program Expanded Abstracts, 5296–5301.

Baykulov, M., and D. Gajewski, 2009, Prestack seismic data enhancement with partial common-reflection-surface (CRS) stack: Geophysics, 74, V49–V58.

Benfield, N., V. Rambaran, J. Dowlath, T. Sinclair, M. Evans, J. Richardson, and A. Irving, 2017, Extracting geologic information directly from high-resolution full-waveform inversion velocity models—A case study from offshore Trinidad: The Leading Edge, 36, 67–74.

Bergler, S., 2004, On the determination and use of kinematic wavefield attributes for 3D seismic imaging: PhD thesis, University of Karlsruhe.

Blacic, T. M., and W. S. Holbrook, 2010, First images and orientation of fine structure from a 3-D seismic oceanography data set: Ocean Science, 6, 431–439.

Bonomi, E., A. M. Cristini, D. Theis, and P. Marchetti, 2009, 3D CRS analysis: A Data-driven optimization for the simultaneous estimate of the eight parameters: SEG Technical Program Expanded Abstracts, 3284–3291.

Dell, S., and D. Gajewski, 2011, Common-reflection-surface-based workflow for diffraction imaging: Geophysics, 76, S187–S195.

Dickinson, A., N. White, and C. Caulfield, 2017, Spatial variation of diapycnal diffusivity estimated from seismic imaging of internal wave field, Gulf of Mexico: Journal of Geophysical Research, 122, 9827–9854.

Dümmong, S., and D. Gajewski, 2008, A multiple suppression method via CRS attribute: SEG Technical Program Expanded Abstract, 2531–2535.

Duveneck, E., 2004, Velocity model estimation with data-derived wavefront attributes: Geophysics, 69, 265–274.

Fortin, F., and S. Holbrook, 2009, Sound speed requirements for optimal imaging of seismic oceanography data: Geophysical Research Letters, 36, L00D01.

Garabito, G., 2018, Global optimization strategies for implementing 3d common-reflection-surface stack using the very fast simulated annealing algorithm: Application to real land data: Geophysics, 83, V253–V261.

Holbrook, W. S., P. Paramo, S. Pearse, and R. Schmitt, 2003, Thermohaline fine structure in an oceanographic front from seismic reflection profiling: Science, 301, 821–824.

Hubral, P., 1983, Computing true amplitude reflections in a laterally inhomogeneous earth: Geophysics, 48, 1051–1062.

Jäger, R., J. Mann, G. H¨ocht, and P. Hubral, 2001, Common-reflection-surface stack: Image and attributes: Geophysics, 66, 97–109.

Klaeschen, D., R. W. Hobbs, G. Krahmann, C. Papenberg, and E. Vsemirnova, 2009, Estimating movement of reflectors in the water column using seismic oceanography: Geophysical Research Letters, 24, L00D03.

Lacombe, C., S. Butt, G. Mackenzie, M. Schons, and R. Bornard, 2009, Correcting for water-column variations: The Leading Edge, 28, 198–201.

MacKay, S., J. Fried, and C. Carvill, 2003, The Impact of water-velocity variations on deepwater seismic data: The Leading Edge, 4, 344–350.

Mann, J., 2002, Extensions and applications of the common-reflection-surface stack method: PhD thesis, University of Karlsruhe.

Mayne, W. H., 1962, Common reflection point horizontal data stacking techniques: Geophysics, 27, 927–938.

Mirshak, R., M. Nedimovi, B. Greenan, B. Ruddick, and L. K., 2010, Coincident reflection images of the Gulf Stream from seismic and hydrographic data: Geophysical Research

Letters, 37, L05602.

Müller, N., 2003, The 3D common-reflection-surface stack - Theory and application: Master's thesis, University of Karlsruhe.

Müller, T., 1999, The common reflection surface stack method: Seismic imaging without knowledge of the velocity model: PhD thesis, University of Karlsruhe.

Nandi, P., W. S. Holbrook, S. Pearse, P. Paramo, and R. W. Schmitt, 2004, Seismic reflection imaging of Norwegian Sea water mass boundaries: Geophysical Research Letters, 31, L23311.

Papenberg, C., D. Klaeschen, G. Krahmann, and R. W. Hobbs, 2010, Ocean temperature and salinity inverted from combined hydrographic and seismic data: Geophysical Research Letters, 37, L04601.

Piete, H., L. Marie, B. Marsset, and Y. Thomas, 2013, Seismic reflection imaging of shallow oceanographic structures: Journal of Geophysical Research, 118, 2329–2344.

Pinheiro, L. M., H. Song, B. Ruddick, J. Dubert, I. Ambar, K. Mustafa, and R. Bezerra, 2010, Detailed 2-D imaging of the Mediterranean outflow and meddies off W iberia from multichannel 442 seismic data: Journal of Marine Systems, 79, 89–100.

Pratt, R. G., 1999, Seismic waveform inversion in the frequency domain. Part 1: Theory and verification in a physical scale model: Geophysics, 64, 888–901.

Ruddick, B., H. Song, C. Dong, and L. Pinheiro, 2009, Water column seismic images as maps of temperature gradient: Oceanography, 22, 192–205.

Schleicher, J., M. Tygel, and P. Hubral, 1993, Parabolic and hyperbolic paraxial two-point traveltimes in 3D media: Geophysical Prospecting, 41, 495–513.

Schwarz, B., 2019, Coherent wavefield subtraction for diffraction separation: Geophysics, 84, V157–V168.

Wood, W. T., W. S. Holbrook, M. K. Sen, and P. L. Stoffa, 2008, Full waveform inversion of reflection seismic data for ocean temperature profiles: Geophysical Research Letters, 35, L04608.

Xie, Y., and D. Gajewski, 2016, Simultaneous estimation of the 3D CRS attributes by an evolutionary-based neldermead algorithm: SEG Technical Program Expanded Abstract, 4326–4330.

———, 2018, 3D wavefront attribute determination and conflicting dip processing: Geophysics, 83, V325–V343.

Yilmaz, O., 2001, Seismic data analysis: Processing, inversion, and interpretation of seismic data: Society of Exploration Geophysicists (SEG).

Figure Captions

Figure 1: The 2D CRS parameters: the incidence angle is denoted by α; R_{NIP} is the radius of curvature of a wavefront emitted by a fictitious point source at the normal incidence point (NIP); R_N is the radius of wavefront curvature of the fictitious so-called normal wave that would be generated normally to the reflector from a region surrounding the normal incidence point. This region represents the common-reflection-surface.

Figure 2: The black curves indicate the prestack traveltimes. The 2D CRS stacking surface is indicated by red. The blue surface indicates the partial 2D CRS stack surface. While the result of CRS stacking is assigned to a zero-offset sample, e.g., the red point (x_0, t_0), the result of partial CRS can be assigned to any offset sample, e.g, the blue point.

Figure 3: Location of the study area in the northern Gulf of Mexico continental shelf. The zoom-in insertion highlights the 3D seismic survey carried out by Wesrne-Geco for oil and gas exploration. The seafloor bathymetry (curtsey from https://www.boem.gov/oil-gas-energy/mapping-and-data/map-gallery/boem-northern-gulf-mexico-deepwater-bathymetry-grid-3d) shows water depth and complex Gulf of Mexico seafloor topography.

Figure 4: Example of an arbitrary CMP gather (a) and the enhanced CRS supergather (b) from the same location.

Figure 5: (a) Original and (b) partial CRS enhanced velocity spectrum of the same CMP gather in the Figure 4(a). The semblance is increased and allows for more reliable picking.

Figure 6: The CMP stack section of an inline extracted in the middle from the stacked volume of (a) and the CRS stack section of the same inline (b). Please note the same gain in both images. Boxes and arrows highlight areas where reflections between (a) and (b) are improved.

Figure 7: Depth converted crossline obtained from CMP (a) and the CRS (b) processing. Please note the same gain in both images. CRS reduce the vertical noise pattern due to acquisition footprint effect.

Figure 8: Three depth slices 350 m (a and b), 650 m (c and d) and 850 m (e and f) are presented to highlight CRS results (b, d and f) versus CMP (a, c, e). The same gain is used in all the images, the red arrows highlight the most significant differences.

Figure 9: Sub portion of the 3D depth volume both for CMP (a) and CRS (b) processing. The size of sub volume is $7.5 \times 6.25 \times 0.4$ km^3 with the depth (vertical axis) stating at 600m. The red arrows highlight the differences.

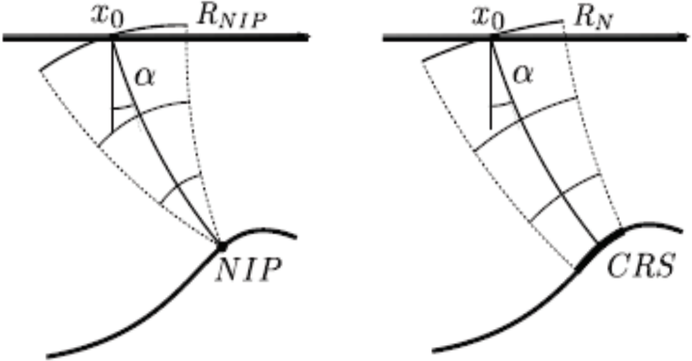
x_0
R_{NIP}
α
NIP
x_0
R_N
α
CRS

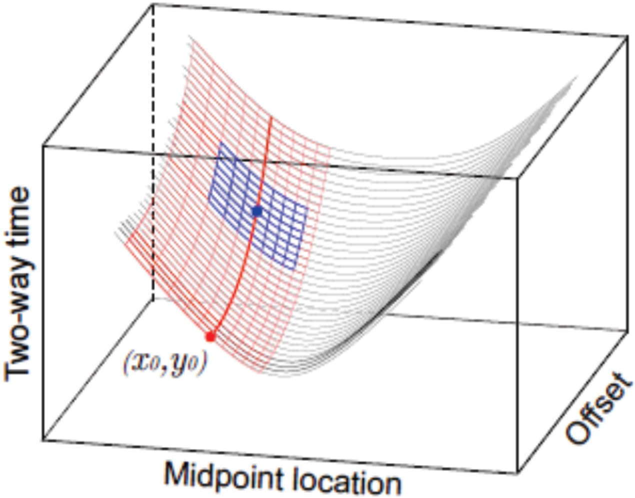
Two-way time
(x_0, y_0)
Offset
Midpoint location

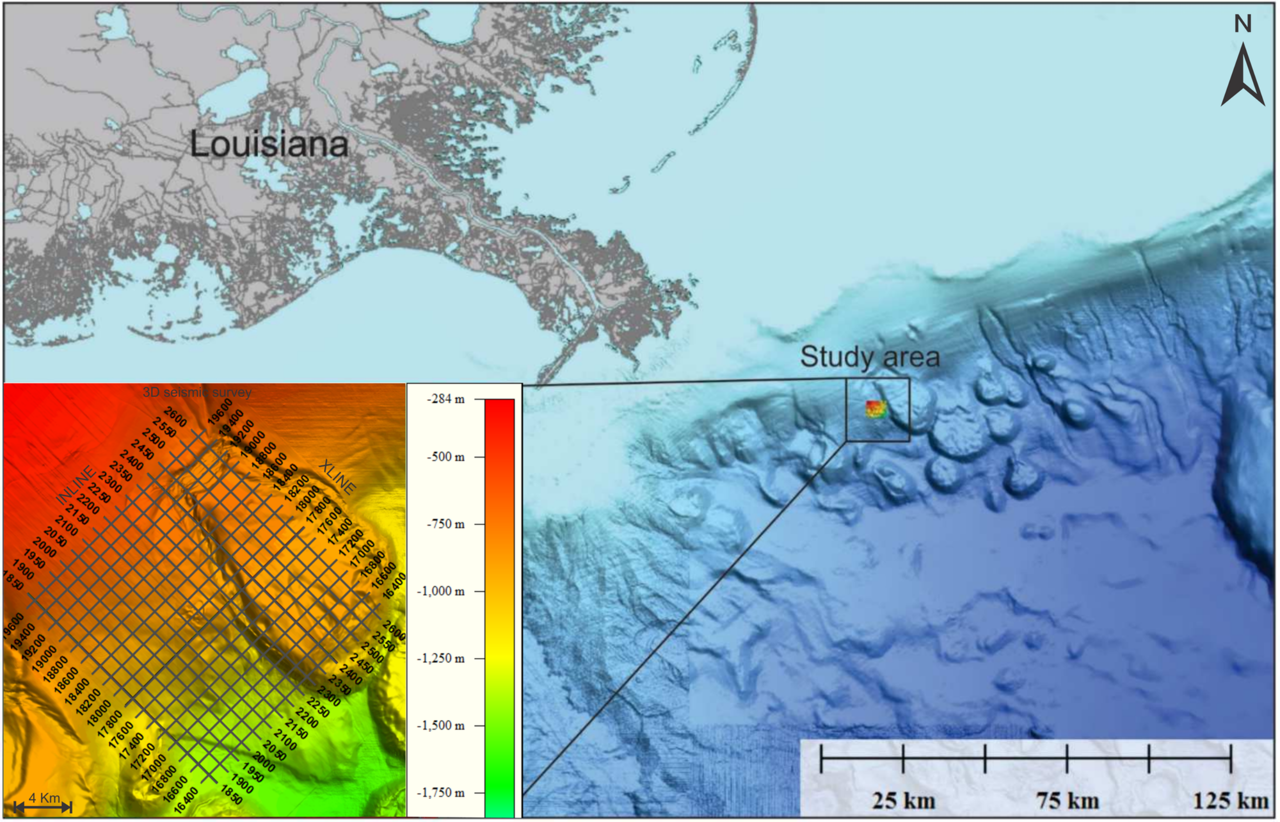
N
Louisiana
Study area
3D seismic survey
INLINE
XLINE
4 Km
-284 m
-500 m
-750 m
-1,000 m
-1,250 m
-1,500 m
-1,750 m
25 km
75 km
125 km

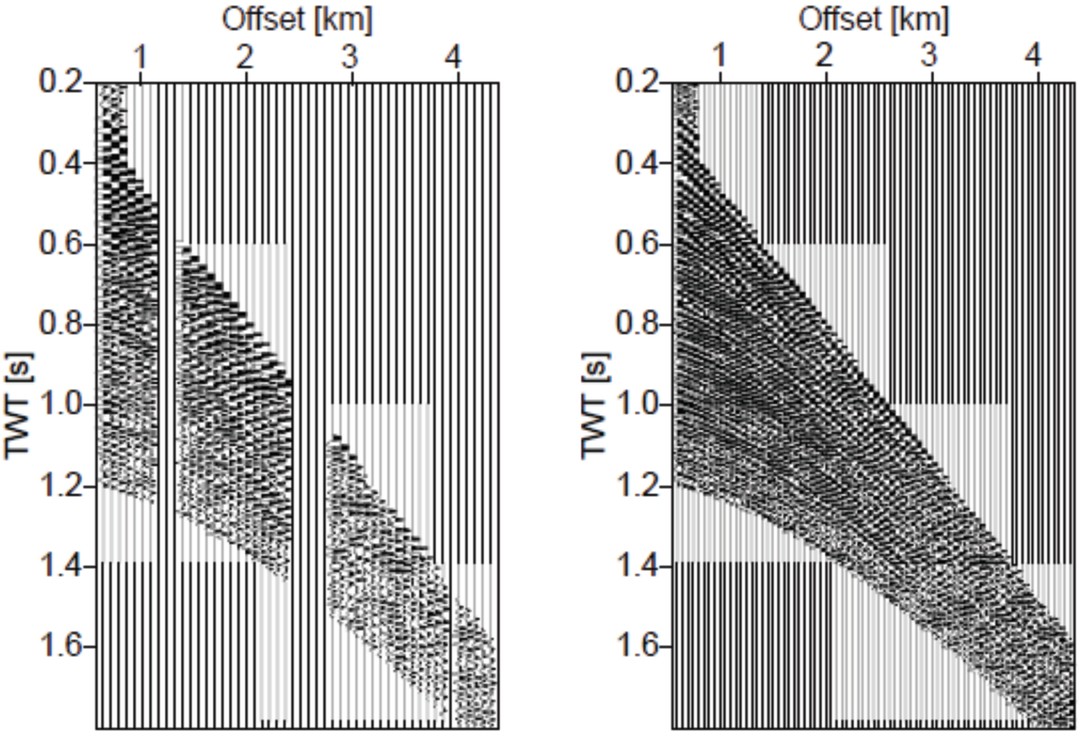
Offset [km]
1
2
3
4
0.2
0.4
0.6
0.8
1.0
1.2
1.4
1.6
TWT [s]
Offset [km]
1
2
3
4
0.2
0.4
0.6
0.8
1.0
1.2
1.4
1.6
TWT [s]

(a) (b)

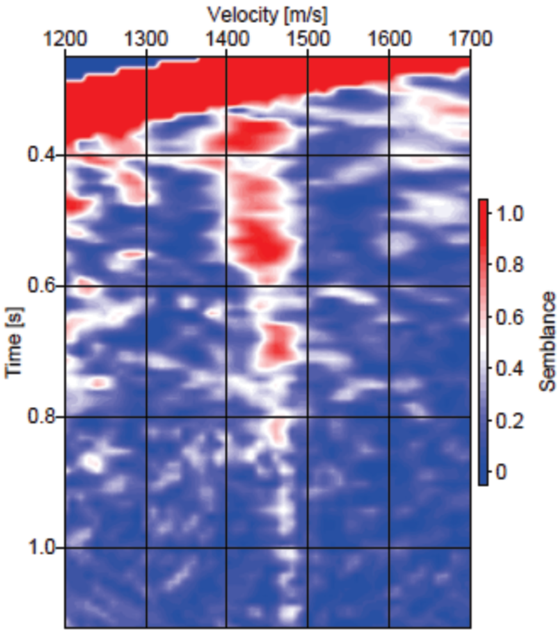
Velocity [m/s]
1200
1300
1400
1500
1600
1700
Time [s]
0.4
0.6
0.8
1.0
Semblance
1.0
0.8
0.6
0.4
0.2
0

(a)

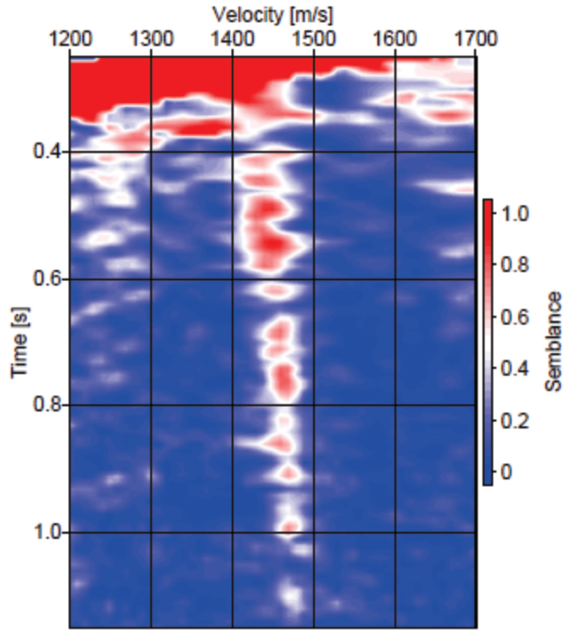
Velocity [m/s]
1200
1300
1400
1500
1600
1700
Time [s]
0.4
0.6
0.8
1.0
Semblance
1.0
0.8
0.6
0.4
0.2
0

(b)

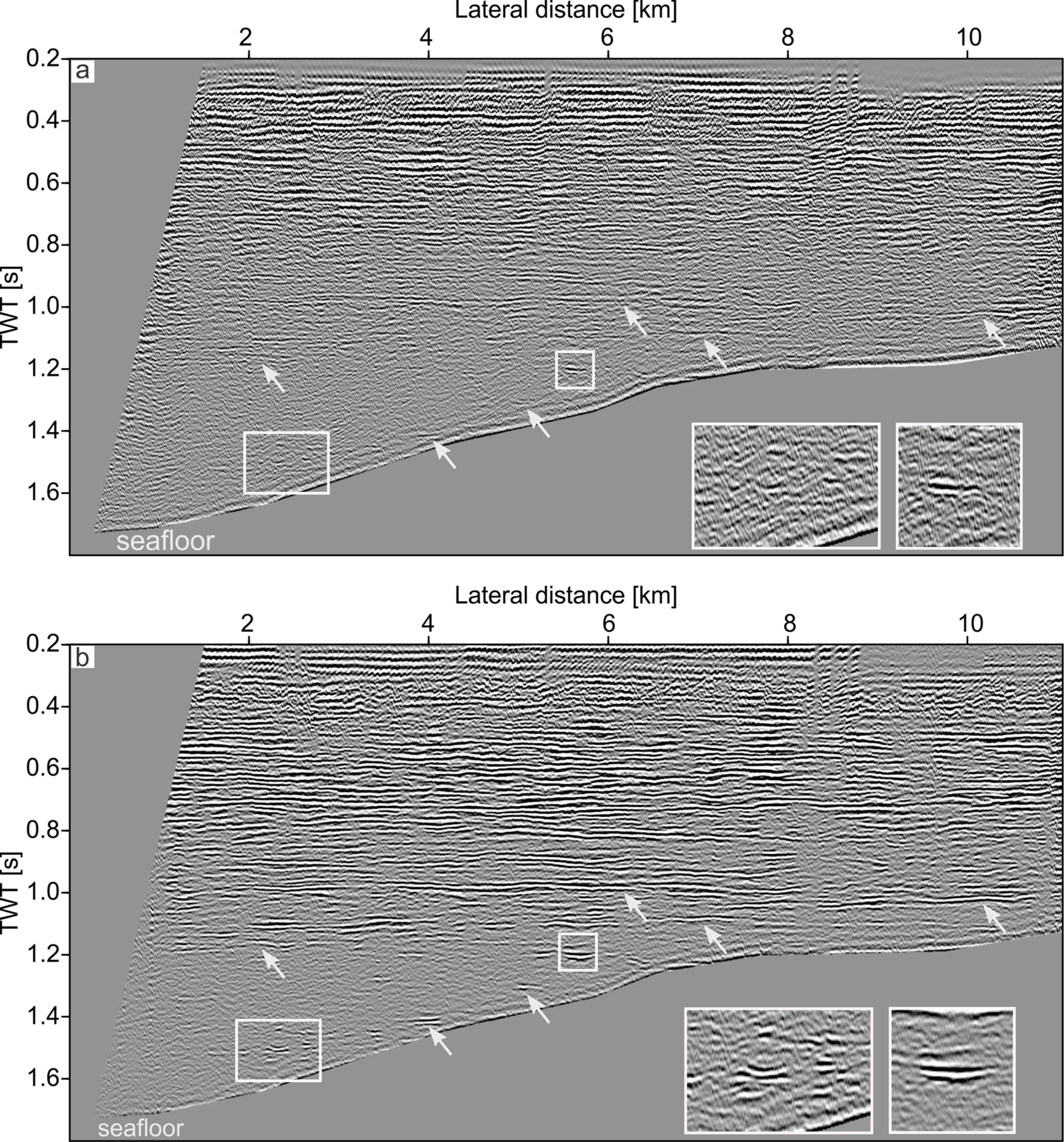
Lateral distance [km]
2
4
6
8
10
0.2
0.4
0.6
0.8
1.0
1.2
1.4
1.6
TWT [s]
a
seafloor
Lateral distance [km]
2
4
6
8
10
0.2
0.4
0.6
0.8
1.0
1.2
1.4
1.6
TWT [s]
b
seafloor

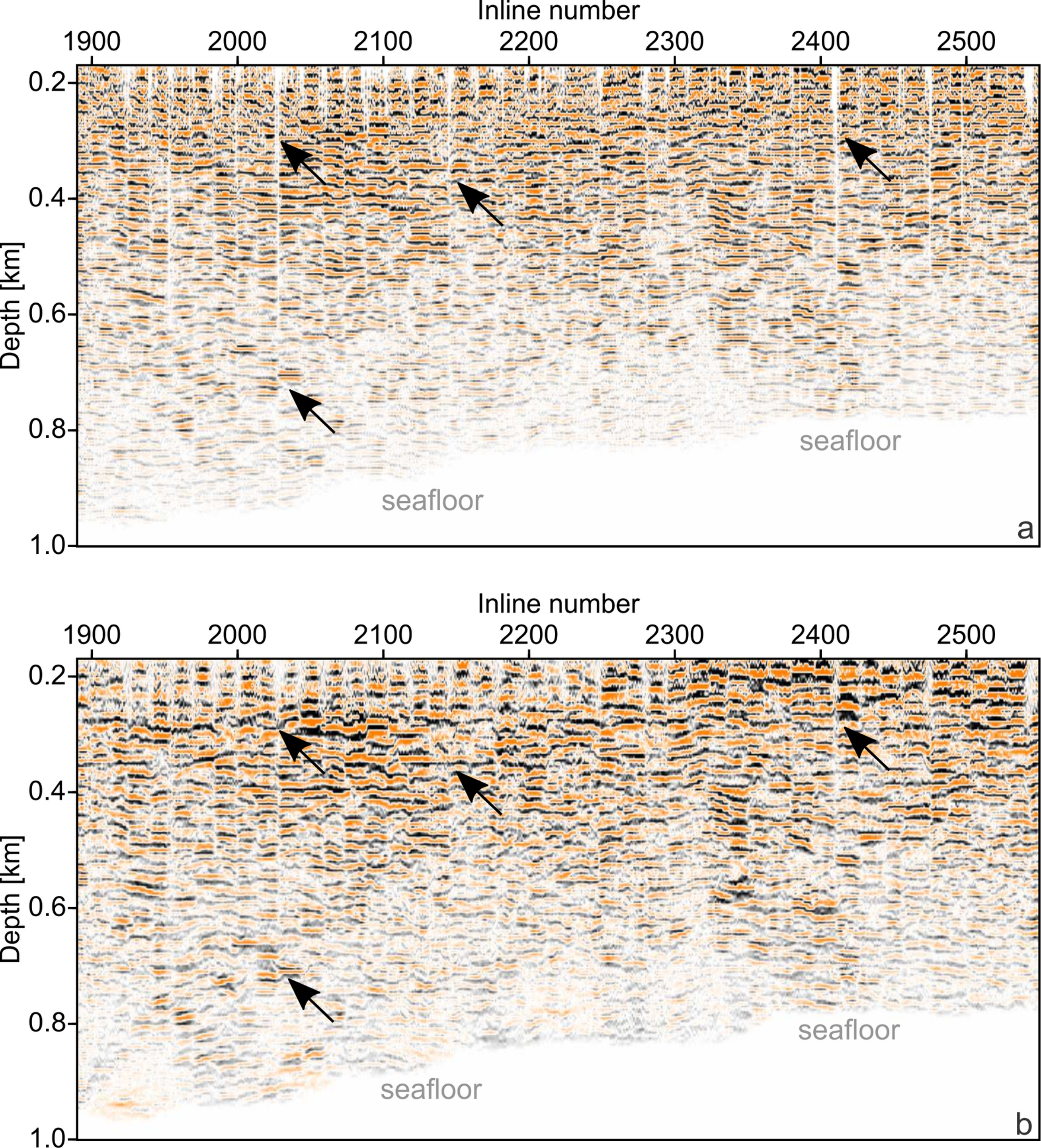

Inline number
1900
2000
2100
2200
2300
2400
2500
Depth [km]
0.2
0.4
0.6
0.8
1.0
seafloor
seafloor
a
Inline number
1900
2000
2100
2200
2300
2400
2500
Depth [km]
0.2
0.4
0.6
0.8
1.0
seafloor
seafloor
b

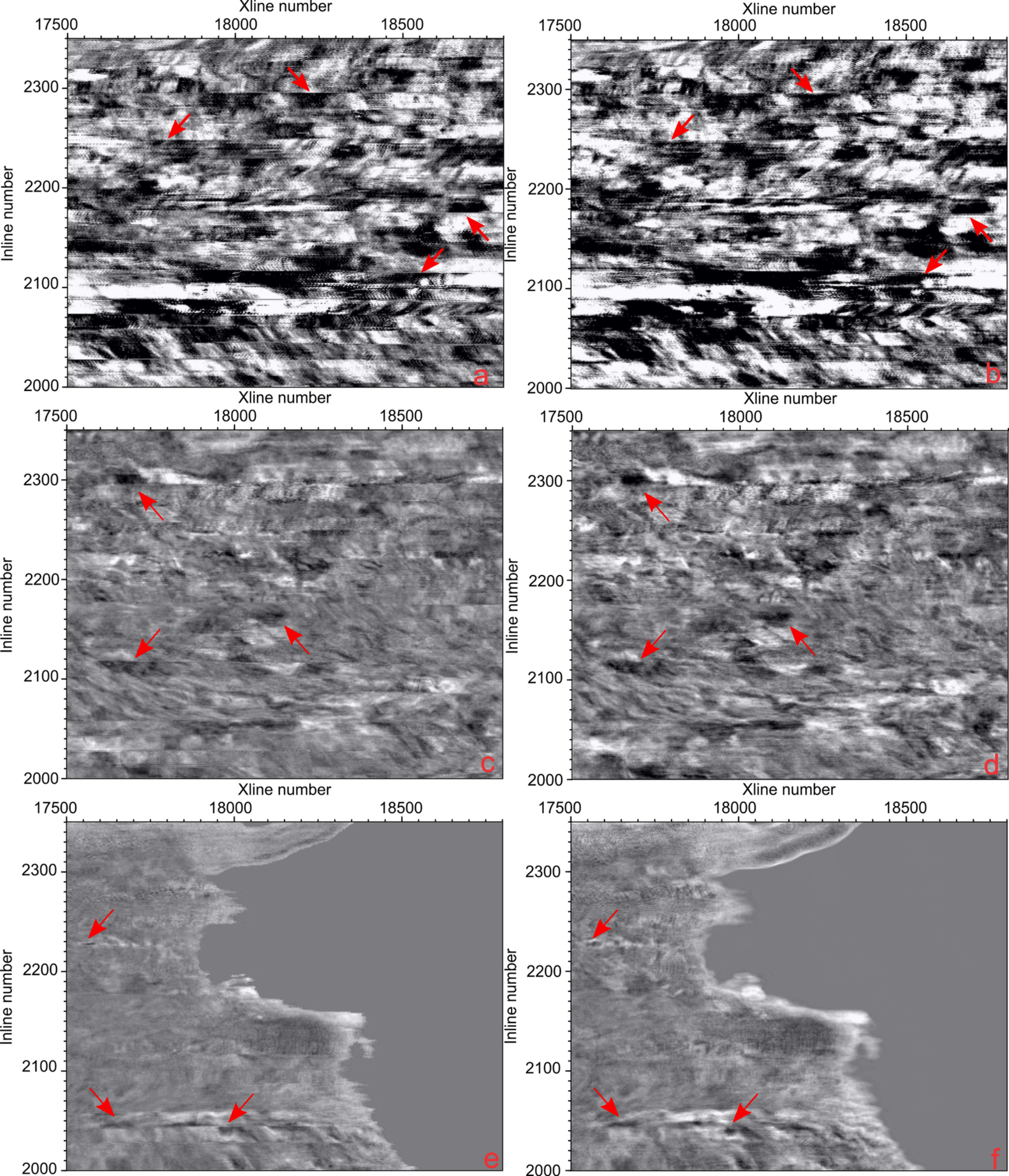
Xline number
17500
18000
18500
Inline number
2300
2200
2100
2000
a
b
c
d
e
f

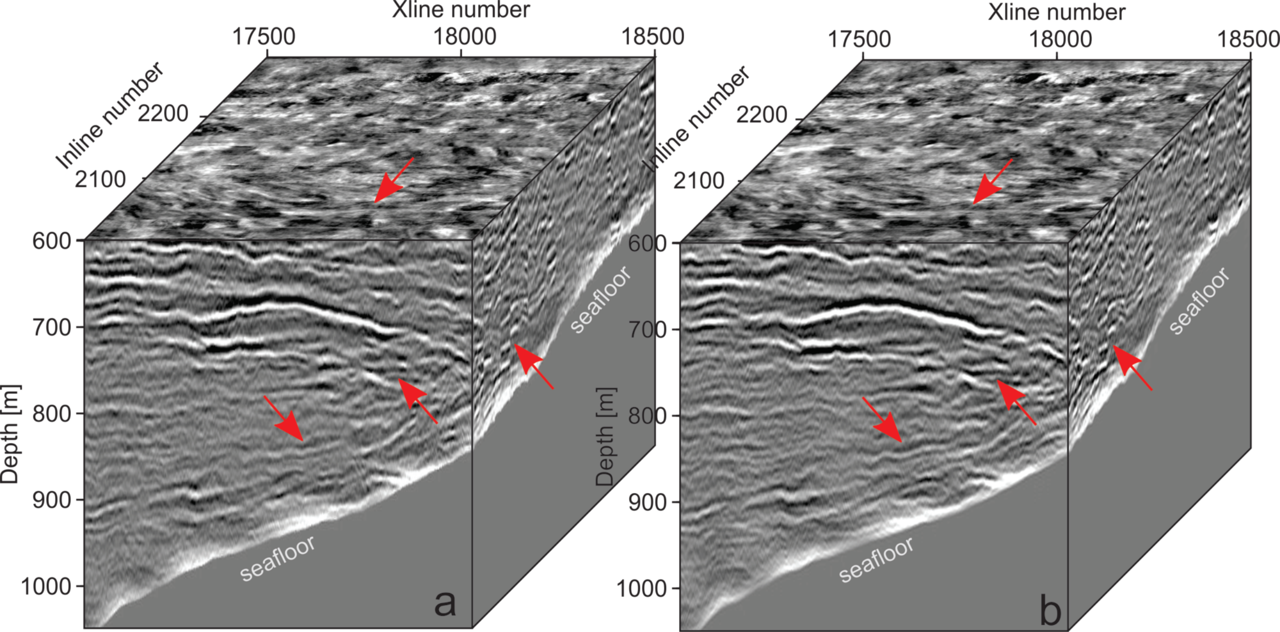
Xline number
17500
18000
18500
Inline number
2200
2100
600
700
800
900
1000
Depth [m]
seafloor
seafloor
a
Xline number
17500
18000
18500
Inline number
2200
2100
600
700
800
900
1000
Depth [m]
seafloor
seafloor
b